

Research Article

A Novel Microstructure of 2-Bit Optical Analog to Digital Converter Based on Kerr Effect Nonlinear Nanocavities in 2D Photonic Crystal

Suliman Ibraheem Shelash Al-Hawary,¹ Ahmed Alkhayat,² M. Mehdi Shafieezadeh ,³ Ngakan Ketut Acwin Dwijendra ,⁴ Eman Khalaf,⁵ and Iskandar Muda⁶

¹Department of Business Administration, Business School, Al al-Bayt University, P.O. BOX 130040, Mafraq 25113, Jordan

²Department of Computer Technical Engineering, College of Technical Engineering, Najaf, Iraq

³Department of Chemical Engineering, Islamic Azad University, Shiraz, Iran

⁴Faculty of Engineering, Udayana University, Bali 80361, Indonesia

⁵Department of Pharmacy, University: Al-Maarif University College, Ramadi, Iraq

⁶Department of Doctoral Program, Faculty Economic and Business, Universitas Sumatera Utara, Medan 20222, Indonesia

Correspondence should be addressed to M. Mehdi Shafieezadeh; shafieezhad.shirazu@gmail.com

Received 1 May 2022; Revised 29 October 2022; Accepted 16 December 2022; Published 6 January 2023

Academic Editor: Chengkuo Lee

Copyright © 2023 Suliman Ibraheem Shelash Al-Hawary et al. This is an open access article distributed under the Creative Commons Attribution License, which permits unrestricted use, distribution, and reproduction in any medium, provided the original work is properly cited.

In this paper, an all-optical analog-to-digital converter based on nonlinear with silicon materials is designed and simulated. The proposed structure consists of three nonlinear nanocavity that control the optical signal power intensity. The nonlinear material used is aluminum gallium arsenide (AlGaAs). Aluminum gallium arsenide (AlGaAs) with a linear refractive index of $n_0 = 1.4$ and a nonlinear refractive index of $n_2 = 1.5 \times 10^{-17}$. Due to the small path length of the waveguides, the optical signals move a short distance and as a result, the power optical losses along the path are reduced and on the other hand, the speed of the structure is increased. The transmission percentage is between 90% and 100%. The overall dimensions of the structure are $324 \mu\text{m}^2$. The plane wave expansion (PWE) method is used to calculate the band structure. The two-dimensional finite difference time domain (2D-FDTD) method is used to calculate the transmission power spectrum and the simulation results.

1. Introduction

Nowadays, optical technology has an essential role to play in the rapid advancement of communication and information technologies [1–8]. Tools that utilize photons rather than electrons as information carriers hold greater speeds and decrease interference light channels [9–16]. A photonic crystal consists of 2 or so materials with various coefficients of permeability, placed next to each other periodically [17–25]. This report presents a fast revision of analog to digital converters based on photonic crystals [26–33]. The mentioned photonic crystal structures hold the capacity to be integrated [34–41] and because of using engineered flaws in their crystal lattice as well as utilizing nonlinear materials, have the capability to limit the light inside [42,

43]. The all-optical analog to digital (A/D) converters available so far is very limited in terms of number [7, 44–49]. Photon crystals have absorbed a lot of attention lately due to their great flexibility in optically integrated circuits, in particular, in controlling light emission [1–3, 8, 10, 50–54]. These crystals are considered an alternate array of dielectrics having the capability of controlling the flow of light by gaps (PBGs). The photonic gap is the range of frequency that the coming light is not permitted to propagate. Those structures are a favorable choice for realizing passive as well as active optical tools. Hence, these crystals are able to be utilized to fabricate and design tools, including switches [55–57], detectors [58, 59], logic gates [3, 35, 37, 60–62], filters [63–70], optical dividers [71–74], and converters [75–79], utilize other numerous applications.

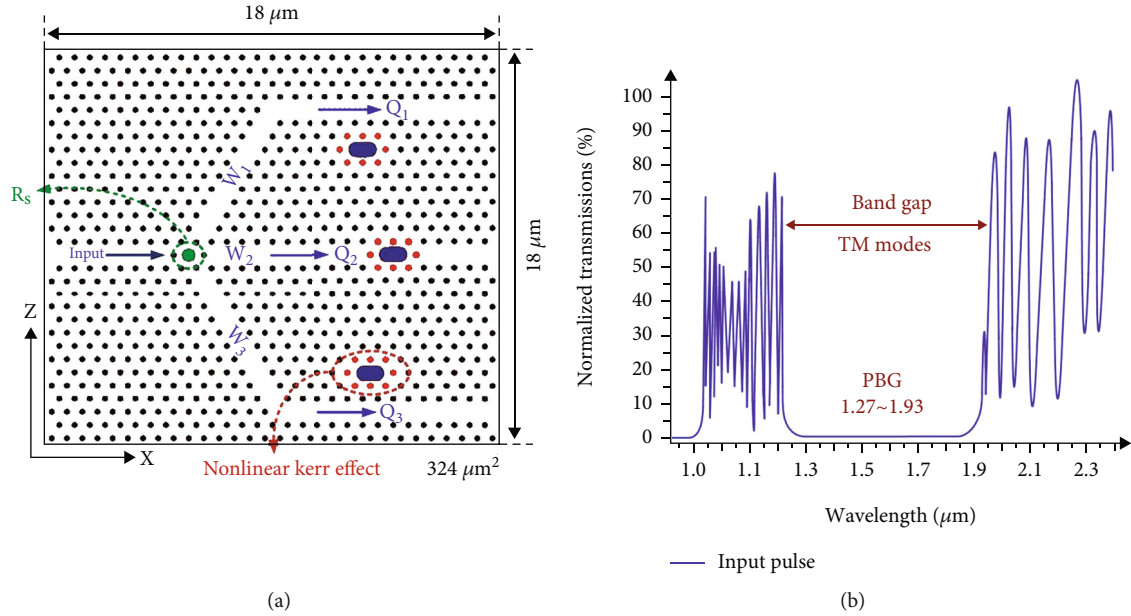


FIGURE 1: (a) The proposed optical structure of two-bit analog-to-digital converter on the basis of nonlinear nanocavities. (b) Display the pulse signal of the input and specify the range of the bandgap.

Several converters offered are on the basis of the optical fibers' nonlinear performance along with a length of about kilometers. It appears highly improbable to integrate those and all-optical converters. Analogs are provided to all-optical digital and have the ability to integrate; quantization has been done using a chalcogenide waveguide. In fact, 2-dimensional photonic crystals are composed of a range of cylinders of infinite length (dielectric) installed in a dielectric substrate (homogeneous). Photonic crystal substrates are designed in two types. The first type of dielectric rods is placed in the air bed, and the second type of air cavities are created in the dielectric bed. If a light beam hits the structure with a frequency equal to the frequency of the light gap, it is emitted without scattering inside the structure.

Youssefi et al. [75] presented a new configuration for an all-optical analog-to-digital converter based on nonlinear materials has been proposed. Mehdizadeh et al. [77, 79] presented a proposed structure that is composed of a nonlinear triplexer and an optical coder. The nonlinear triplexer is for creating discrete levels in the continuous optical input signal, and the optical coder is for generating a 2-bit standard binary code out of the discrete levels coming from the nonlinear triplexer. Controlling the resonant mode of the resonant rings through optical intensity is the main objective and working mechanism of the proposed structure. The maximum delay time obtained for the proposed structure was about 5 ps and the total footprint is about $1520 \mu\text{m}^2$. In other research presented [78], a novel design for realizing all optical analog to digital converter will be proposed.

Recently, in 2020, Hosseinzadeh Sani et al. proposed a 2-bit all-optical analog-to-digital converter [80]. In this converter, nonlinear ring resonators are used. The transmission power is between 65%~90% and the structure dimensions are $777.52 \mu\text{m}^2$. In the following year, 2021, Chen et al. proposed a 5-bit all-optical analog-to-digital converter [81], in

which the number of bits was important, the subparameters, such as dimensions, increased greatly and the transmission decreased greatly. Dimensions in this structure are equal to $1796 \mu\text{m}^2$. According to the work done, it can be concluded that in analog-to-digital converters, in addition to the number of bits, the amount of transmission power and the dimensions of the structure are also important [82–85].

In this article, in addition to the two-bit structure, an attempt is made to reduce the dimensions of the structure, which in turn increases the speed of the structure. On the other hand, the percentage of power transmission is between 90%~100%, which, when the percentage of transmission is 100%, it means that the power loss of the optical signal in the structure is almost 0%. The general structure of the article consists of five main sections. In the first part, photonic crystals are introduced, and the design of all converters in the photonic crystal bed is discussed. In addition, an overview of the work of the last two years has been done and the problems and challenges have been examined. In the second part, materials and methods are discussed. In this part, the nonlinear behavior of materials, and the number of different optical powers in photonic crystal structures are explained. In the third part, the proposed structure is designed. In the fourth section, the simulation results are discussed; and finally, in the fifth chapter, the conclusion is made.

2. Materials and Methods

In a structure utilizing nonlinear materials along with the Kerr effect, besides to determining the linear section of the material, the behavior of nonlinearity should be defined as well. The Kerr effect is a promising nonlinearity as it means a near-instantaneous intensity dependent refractive index change. Equation (1) can be used in order to acquire the

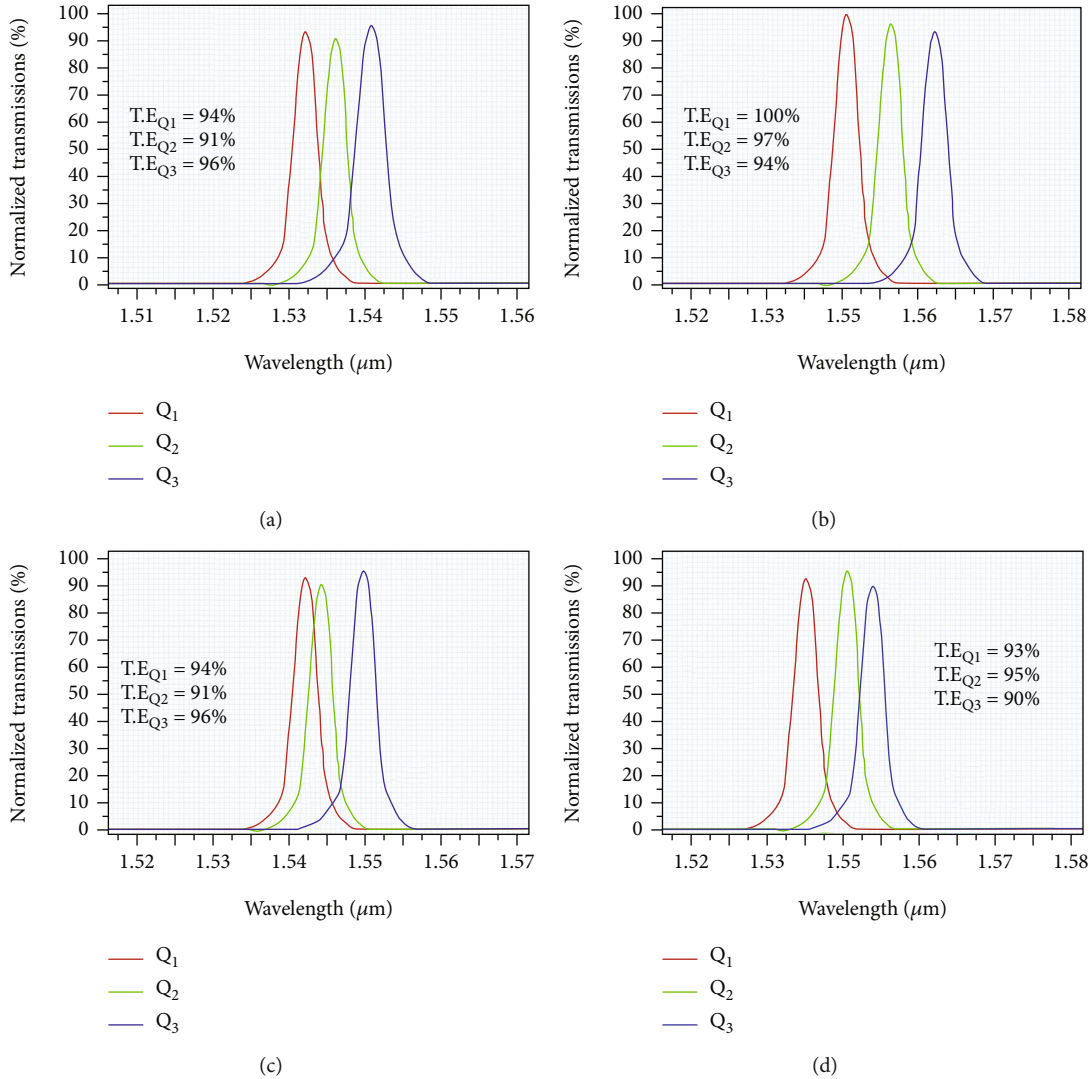


FIGURE 2: Normalized transmission wavelengths from the output ports when the input power is at, (a) $0 < P_{in} < 0.25P_0$, (b) $0.25P_0 < P_{in} < 0.5P_0$, (c) $0.5P_0 < P_{in} < 0.75P_0$, (d) $0.75P_0 < P_{in} < P_0$.

TABLE 1: Different values of resonant wavelength for input power intensities at, (a) $0 < P_{in} < 0.25P_0$, (b) $0.25P_0 < P_{in} < 0.5P_0$, (c) $0.5P_0 < P_{in} < 0.75P_0$, (d) $0.75P_0 < P_{in} < P_0$.

P_{in} ($W/\mu m^2$), $P_0 = 1$ W	Q ₁ [λ (μm)]	Q ₂ [λ (μm)]	Q ₃ [λ (μm)]
$0 < P_{in} < 0.25P_0$	1.531	1.536	1.541
$0.25P_0 < P_{in} < 0.5P_0$	1.550	1.556	1.563
$0.5P_0 < P_{in} < 0.75P_0$	1.542	1.544	1.550
$0.75P_0 < P_{in} < P_0$	1.545	1.550	1.554

nonlinear refractive index of several materials. N represents the whole value of the refractive index at a specific power. n_0 represents the refractive index of the linear section of the material in question. n_2 is the index of the nonlinear section of the material, changing with changes in the intensity of light (field square), parameter I represent the light signal's

intensity. The change in the refractive index named the optical chorus effect due to the fact that it seems kind of similar to the electrostatic impact of a chorus when the refractive index of a material with a static electric field's square applied to it changes [80].

$$n = n_0 + n_2 I. \quad (1)$$

So as to attain the light field intensity, Equation (2) is used. As observed in Equation (2), the light field' intensity differs according to the square of the field. Also, C represents the light speed in air.

$$I = 2n_0 \epsilon_0 c |E(\omega)|^2, \quad (2)$$

$$n_2 = \frac{3}{4n_0^2 \epsilon_0 c} \chi^{(3)}. \quad (3)$$

Equation (3) shows the nonlinear refractive index of the

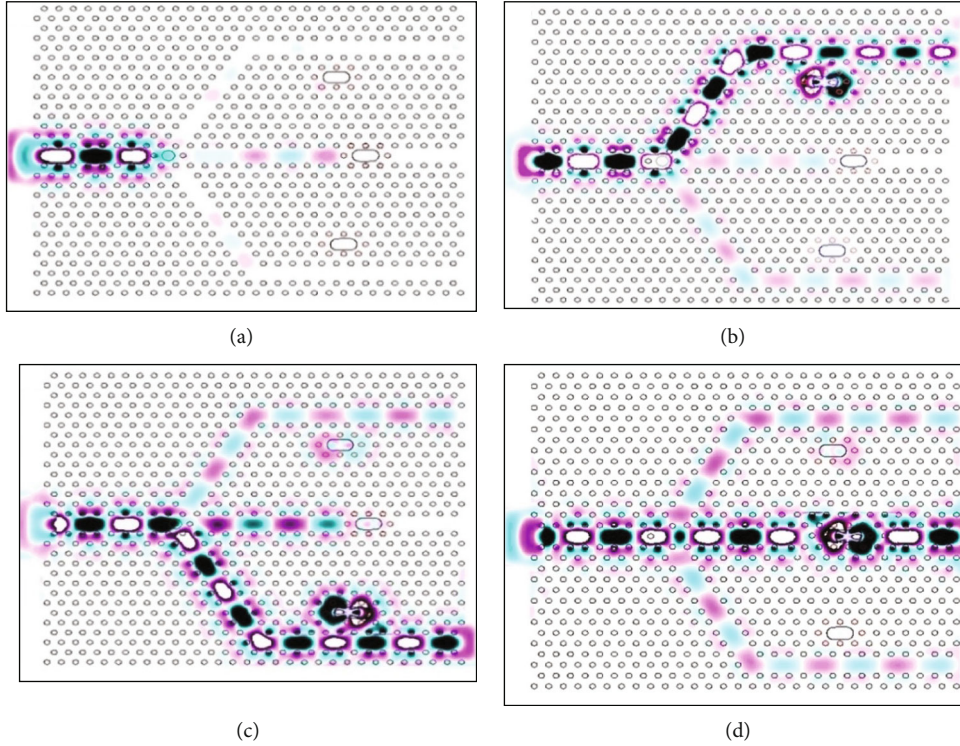


FIGURE 3: The behavior of the electric field for different input intensities at, (a) $0 < P_{in} < 0.25P_0$, (b) $0.25P_0 < P_{in} < 0.5P_0$, (c) $0.5P_0 < P_{in} < 0.75P_0$, (d) $0.75P_0 < P_{in} < P_0$.

material. Decreasing or increasing both parameters can change the total refractive index of the material at a specific intensity [80].

3. Proposed Structure of ADC

Over the proposed structure, silicon dielectric rods with refractive index of $n_1 = 3.6$ placed in the air bed with a refractive index of $n_g = 1$. The mentioned structure is two-dimensions and a hexagonal lattice. The dielectric rods on the X-Z plate have a number of 30×30 , and the lattice index value $a = 600$ nm is selected. Figure 1(a) shows the proposed structure of the all-optical analog-to-digital converter. In Figure 1(a), can be seen different states of placement of nanocavities, as it can be seen that nanocavities can be placed in different places relative to the movement of the photonic crystals. To acquire the best radius of the dielectric rods that maximize the photonic bandgap, the diagram of the photonic bandgap regarding filling (r/a) is used for the TM polarization mode utilizing the plane wave expansion (PWE) technique. The filling ratio $isr/a = 0.2$ and the widest band range is between $a/\lambda = 0.31 \sim 0.47$ [86, 87]. Figure 1(b) shows the polarization mode and bandgap for a Gaussian pulse input to the structure.

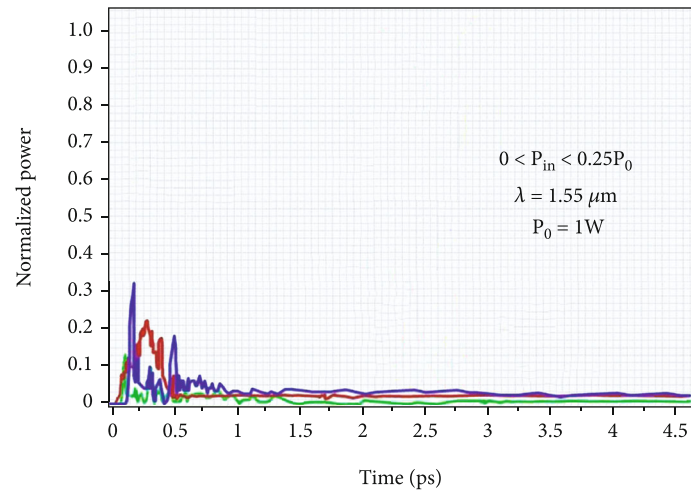
4. Result and Discussion

Simulating is carried out in two major sections; the initial one is applied to the inputs of the nanocavities by imple-

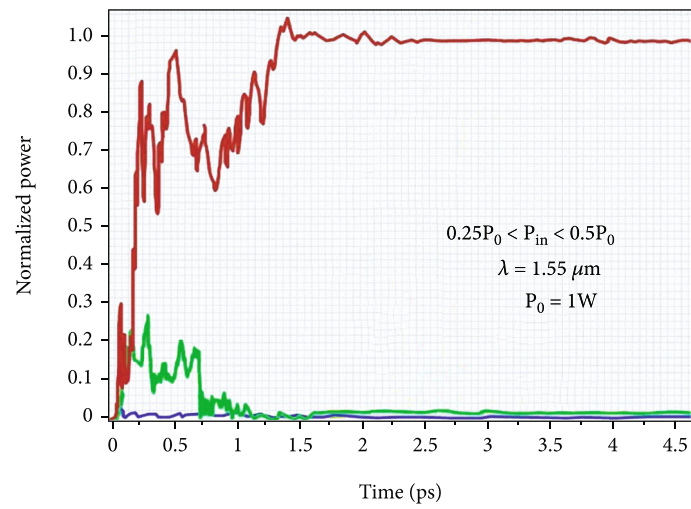
mentation waves to the input port. In the second section, the main outputs of the converter are investigated regarding the nanocavities outputs.

Over the first section, the signal of input light signal is applied as a Gaussian pulse with various powers to the structure's input waveguide and the frequency spectrum (normalized) with a range of specified wavelengths is defined via the charge factor r/a , as illustrated in Figure 2. The normalized transmission wavelengths for the three nanocavities output ports are specified since P_0 is equal to W_1 , in Figure 2(a), while the signal of the input light power covers the range $0 < P_{in} < 0.25P_0$. The waveguides did not pass through the input wavelength $\lambda = 1.55 \mu\text{m}$ (Figure 2(b)). When the power of input light is implemented to the structure among the range of $0.25P_0 < P_{in} < 0.5P_0$, the resonant frequency of the Q_1 channel nanocavities transmits the input light signal's central wavelength to the channel (corresponding). The optical signal power is within the range $0.5P_0 < P_{in} < 0.75P_0$ according to Figure 2(c), where the transmission of the central wavelength by the nanocavities connected to the channel Q_3 is done. In the last step (Figure 2(d)) while the input optical signal's input range is $0.75P_0 < P_{in} < P_0$, the nanocavities resonant frequency of the Q_2 channel gets past the input optical signal's central wavelength. The wavelengths going past through main channel outputs for various normalized input power are demonstrated in Table 1.

As shown in Figure 2, the nonlinear behavior of the analog-to-digital converter is demonstrated in the different input signal's field intensities. To display those shapes, the

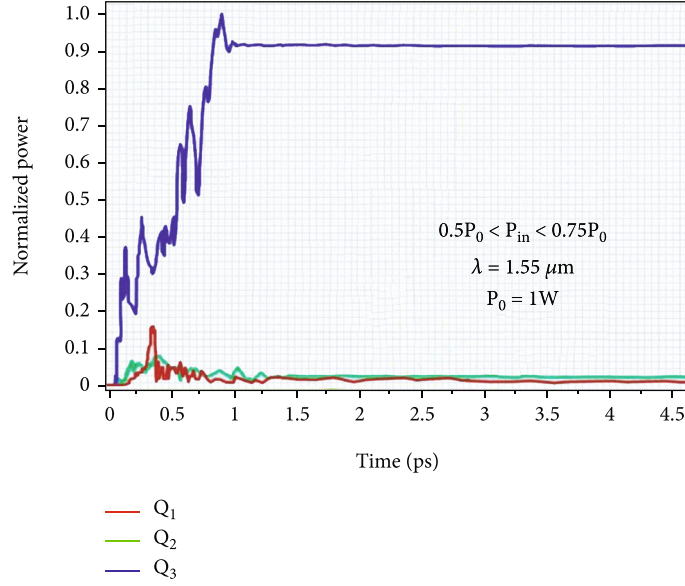


(a)

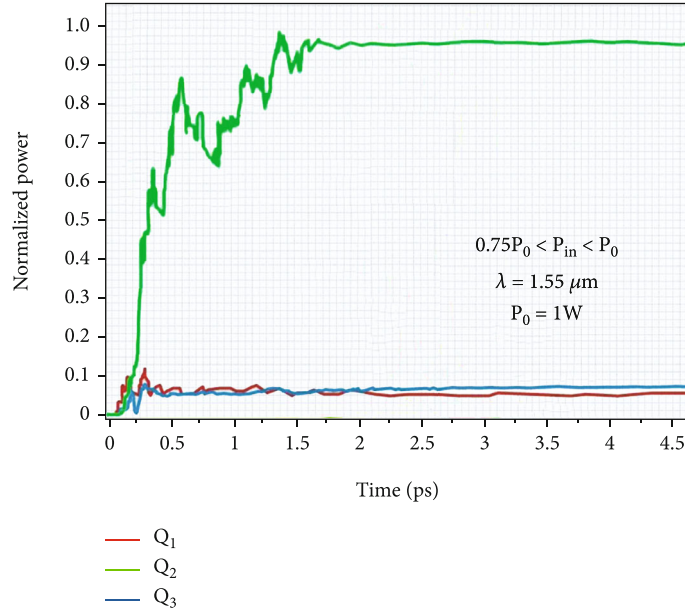


(b)

FIGURE 4: Continued.



(c)



(d)

FIGURE 4: Normalized transmission power spectrum from the output ports of transducer resonant nano-cavities at central wavelength $\lambda = 1.55 \mu\text{m}$.

TABLE 2: Normalized output power in different power intensities.

$P_{\text{in}} (W/\mu\text{m}^2), P_0 = 1 \text{ W}$	Q_1 (%)	Q_2 (%)	Q_3 (%)
$0 < P_{\text{in}} < 0.25P_0$	4	2	6
$0.25P_0 < P_{\text{in}} < 0.5P_0$	100	0	0
$0.5P_0 < P_{\text{in}} < 0.75P_0$	3	5	92
$0.75P_0 < P_{\text{in}} < P_0$	4	91	5

wavelength of the input has to be arranged equally to $\lambda = 1.55 \mu\text{m}$. At each stage, the input light signal's source power is altered. The nonlinear material utilized in nanocavities

differs with respect to changes in input field strength. The signal of the input light is implemented to the input waveguide as a continuous Gaussian wave. If the input signal source power is among the range $0 < P_{\text{in}} < 0.25P_0$, not any of the output channels has a signal. Perform absorbs light and changes the resonance frequency. While the strength of the input signal is implemented to the structure among $0.25P_0 < P_{\text{in}} < 0.5P_0$, the nanowire connected to the W_1 channel gets past the central $\lambda = 1.55 \mu\text{m}$. In case the input source power is within the range $0.5P_0 < P_{\text{in}} < 0.75P_0$, the W_3 channel nanocavity gets past the input signal's central wavelength, and in the last step, the source power between

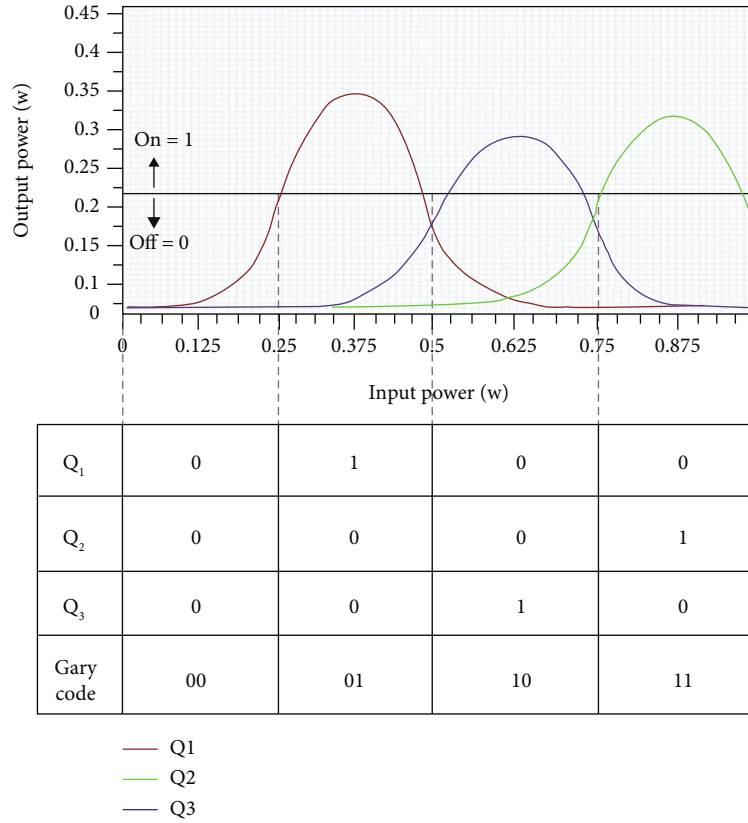


FIGURE 5: The diagram of the input power of the proposed structure based-on output power.

TABLE 3: Comparison of important parameters of the analog-to-digital dual-bit converter with recent articles.

Works	S (μm^2)	Transfers (%)	Years
Ref [75]	449	76	2012
Ref [77]	1520	—	2017
Ref [78]	924	80	2017
Ref [79]	806	60	2018
Ref [80]	777.52	90	2020
This work	324	90	—

$0.75P_0 < P_{in} < P_0$ is applied to the structure. The central wavelength to the structure's main output is transmitted by the W_2 channel. If nonlinear materials are employed in the structure, it implies that the material in question, besides holding a linear part, has a nonlinear part. The linear behavior of materials is actually a scattering action, and the materials' nonlinear behavior shows the adsorption action, in which some desired wavelengths, the material's nonlinear behavior neutralizes the linear behavior of the same material, and the state maintains the waveform after a while.

To find the appropriate wavelengths' range to be utilized as input wavelengths, it appears crucial to determine the normalized transmission power spectrum according to the different fields' intensity from the output ports for particular input power. Then, so as to determine the converter's trans-

fer spectrum, the Fourier transform's output is taken. The power spectrum which is normalized within the wavelengths' range that meet our desired power distribution circumstances, is shown in Figure 3. The input power ratio is broken down into four sections. As shown in Figure 4(a), when the input wave signal strength is placed within the range of section 1, the amount of transmission power seen at all 3 nano-cavities outputs reaches nearly 12% ($Q_1=4\%$, $Q_2=2\%$, $Q_3=6\%$). Figure 4(b) shows that the range of input signal power is set within the power range of section 2. In this case, the power transmitted to channel Q_1 has a value of 100% of the input as well as the output power of Q_2 and Q_3 channels are almost 0% ($Q_2=0\%$, $Q_3=0\%$). In case the input power range is in section 3, the power transmitted to Q_3 channel is 92% of the power of the input, and the powers seen in Q_1 and Q_2 channels are nearly equal to 8% ($Q_1=4\%$, $Q_2=5\%$) (Figure 4(c)). In the last section, which is shown in Figure 4(d), the power range is in section 4, where the Q_2 channel output power is 91%. In addition, the output power of Q_1 and Q_3 channels is roughly 9% ($Q_1=4\%$, $Q_3=5\%$). As observed in the results, due to utilizing the nano-cavities as a hexagonal structure and utilizing non-linear materials in the spots needed for wave transmission, and utilizing proper radii of coupled dielectrics between waveguides and nano-cavities, it has been found that the amount of power loss in the channels that are not used is quite low and the amount of power transferred from the desired channel's input to output is considerable and with inconsequential losses (Table 2).

As shown in Figure 5, the proposed structure's input power diagram is plotted regarding output power for the three channels. When the power is in the first section, the received coding will be "00". If the range of the power is set in the second section, the amount of power in the outputs is $Q_1 = 1$, $Q_2 = 0$, and $Q_3 = 0$, which indicates the coding of "01". In case the range of the power is within the third section, the amount of power in the outputs is $Q_1 = 0$, $Q_2 = 0$ and $Q_3 = 1$, which represent the coding of "10", and in the last section, when the power interval is in the fourth part, the amount of power in the outputs is $Q_1 = 0$, $Q_2 = 1$ and $Q_3 = 0$, which indicate the "11" coding. Thus, the outputs of the cover structure are four logic modes for an analog-to-digital bit converter.

Comparison of important parameters of the analog-to-digital dual-bit converter with recent articles are illustrated in Table 3.

5. Conclusion

In this work, the proposed structure consists of three nanocavities with nonlinear materials. Due to the small size of the photonic crystal substrate, there is no integration problem. The main function of the structure is based on nonlinear nanocavities made of aluminum gallium arsenide (AlGaAs). These parameters are obtained for the proposed structure with dimensions of $324 \mu\text{m}^2$. The output power spectrum that produces the converter logic is calculated using the finite difference time domain method (FDTD). The speed of input power to output waveguides allows this structure to be used in applications with high signal processing speed and accuracy.

Data Availability

There is no data.

Conflicts of Interest

The authors declare no conflict of interest.

References

- [1] Y. Zhang, Y. He, H. Wang, L. Sun, and Y. Su, "Ultra-broadband mode size converter using on-chip metamaterial-based Luneburg lens," *ACS Photonics*, vol. 8, no. 1, pp. 202–208, 2021.
- [2] J. Zuo and X. Lin, "High-power laser systems," *Laser & Photonics Reviews*, vol. 16, no. 5, p. 2100741, 2022.
- [3] L. Kong and G. Liu, "Synchrotron-based infrared microspectroscopy under high pressure: an introduction," *Matter and Radiation at Extremes*, vol. 6, no. 6, article 068202, 2021.
- [4] L. Dai, H. Bian, L. Wang, M. Potier-Ferry, and J. Zhang, "Pre-stress loss diagnostics in pre-tensioned concrete structures with corrosive cracking," *Journal of Structural Engineering*, vol. 146, no. 3, article 04020013, 2020.
- [5] M. Yafei, G. Zhongzhao, W. Lei, and Z. Jianren, "Probabilistic life prediction for reinforced concrete structures subjected to seasonal corrosion-fatigue damage," *Journal of Structural Engineering*, vol. 146, no. 7, article 04020117, 2020.
- [6] L. Wang, D. Lizhao, B. Hanbing, Y. Ma, and Z. Jianren, "Concrete cracking prediction under combined prestress and strand corrosion," *Structure and Infrastructure Engineering*, vol. 15, no. 3, pp. 285–295, 2019.
- [7] Y. Zhang, C. Li, H. Ji et al., "Analysis of grinding mechanics and improved predictive force model based on material-removal and plastic-stacking mechanisms," *International Journal of Machine Tools and Manufacture*, vol. 122, pp. 81–97, 2017.
- [8] M. Yang, C. Li, Y. Zhang et al., "Maximum undeformed equivalent chip thickness for ductile-brittle transition of zirconia ceramics under different lubrication conditions," *International Journal of Machine Tools and Manufacture*, vol. 122, pp. 55–65, 2017.
- [9] J. Zhang, J. Sun, J. Wang, Z. Li, and X. Chen, "An object tracking framework with recapture based on correlation filters and Siamese networks," *Computers and Electrical Engineering*, vol. 98, article 107730, 2022.
- [10] T. Gao, C. Li, Y. Zhang et al., "Dispersing mechanism and tribological performance of vegetable oil-based CNT nanofluids with different surfactants," *Tribology International*, vol. 131, pp. 51–63, 2019.
- [11] Y. Zhang, C. Li, D. Jia et al., "Experimental study on the effect of nanoparticle concentration on the lubricating property of nanofluids for MQL grinding of Ni-based alloy," *Journal of Materials Processing Technology*, vol. 232, pp. 100–115, 2016.
- [12] Z. Xu, C. Xu, J. Xu, and X. Meng, "A computationally efficient authentication and key agreement scheme for multi-server switching in WBAN," *International Journal of Sensor Networks*, vol. 35, no. 3, pp. 143–160, 2021.
- [13] J. Wang, B. Wei, J. Zhang, X. Yu, and P. K. Sharma, "An optimized transaction verification method for trustworthy blockchain-enabled IIoT," *Ad Hoc Networks*, vol. 119, article 102526, 2021.
- [14] Z. Xia, X. Mao, K. Gu, and W. Jia, "Two-dimensional behavior-marker-based data forwarding incentive scheme for fog-computing-based SIOVs," *IEEE Transactions on Computational Social Systems*, vol. 9, no. 5, pp. 1406–1418, 2022.
- [15] W. Wang, X. Huang, J. Li, P. Zhang, and X. Wang, "Detecting COVID-19 patients in X-ray images based on MAI-nets," *International Journal of Computational Intelligence Systems*, vol. 14, no. 1, pp. 1607–1616, 2021.
- [16] B. Li, C. Li, Y. Zhang et al., "Heat transfer performance of MQL grinding with different nanofluids for Ni-based alloys using vegetable oil," *Journal of Cleaner Production*, vol. 154, pp. 1–11, 2017.
- [17] S. Guo, C. Li, Y. Zhang et al., "Experimental evaluation of the lubrication performance of mixtures of castor oil with other vegetable oils in MQL grinding of nickel-based alloy," *Journal of Cleaner Production*, vol. 140, pp. 1060–1076, 2017.
- [18] B. Pu, K. Li, S. Li, and N. Zhu, "Automatic fetal ultrasound standard plane recognition based on deep learning and IIoT," *IEEE Transactions on Industrial Informatics*, vol. 17, no. 11, pp. 7771–7780, 2021.
- [19] K. Li, X. Tang, and K. Li, "Energy-efficient stochastic task scheduling on heterogeneous computing systems," *IEEE Transactions on Parallel and Distributed Systems*, vol. 25, no. 11, pp. 2867–2876, 2014.
- [20] Y. Chen, K. Li, W. Yang, G. Xiao, X. Xie, and T. Li, "Performance-aware model for sparse matrix-matrix multiplication on the sunway taihulight supercomputer," *IEEE Transactions on Parallel and Distributed Systems*, vol. 30, no. 4, pp. 923–938, 2019.

- [21] K. Li, X. Tang, B. Veeravalli, and K. Li, "Scheduling precedence constrained stochastic tasks on heterogeneous cluster systems," *IEEE Transactions on Computers*, vol. 64, no. 1, pp. 191–204, 2015.
- [22] M. Duan, K. Li, X. Liao, and K. Li, "A parallel multiclassification algorithm for big data using an extreme learning machine," *IEEE Transactions on Neural Networks and Learning Systems*, vol. 29, no. 6, pp. 2337–2351, 2018.
- [23] Y. Wang, C. Li, Y. Zhang et al., "Experimental evaluation of the lubrication properties of the wheel/workpiece interface in MQL grinding with different nanofluids," *Tribology International*, vol. 99, pp. 198–210, 2016.
- [24] T. Gao, C. Li, D. Jia et al., "Surface morphology assessment of CFRP transverse grinding using CNT nanofluid minimum quantity lubrication," *Journal of Cleaner Production*, vol. 277, article 123328, 2020.
- [25] X. Zhou, K. Li, Y. Zhou, and K. Li, "Adaptive processing for distributed skyline queries over uncertain data," *IEEE Transactions on Knowledge and Data Engineering*, vol. 28, no. 2, pp. 371–384, 2016.
- [26] T. Xiaoyong, K. Li, Z. Zeng, and B. Veeravalli, "A novel security-driven scheduling algorithm for precedence-constrained tasks in heterogeneous distributed systems," *IEEE Transactions on Computers*, vol. 60, no. 7, pp. 1017–1029, 2011.
- [27] Y. Xu, K. Li, L. He, and T. K. Truong, "A DAG scheduling scheme on heterogeneous computing systems using double molecular structure-based chemical reaction optimization," *Journal of Parallel and Distributed Computing*, vol. 73, no. 9, pp. 1306–1322, 2013.
- [28] X. Tang, K. Li, M. Qiu, and E. H. M. Sha, "A hierarchical reliability-driven scheduling algorithm in grid systems," *Journal of Parallel and Distributed Computing*, vol. 72, no. 4, pp. 525–535, 2012.
- [29] J. Chen, K. Li, K. Li, P. S. Yu, and Z. Zeng, "Dynamic planning of bicycle stations in dockless public bicycle-sharing system using gated graph neural network," *ACM Transactions on Intelligent Systems and Technology*, vol. 12, no. 2, pp. 1–22, 2021.
- [30] Y. Zhang, C. Li, D. Jia, D. Zhang, and X. Zhang, "Experimental evaluation of the lubrication performance of MoS₂/CNT nanofluid for minimal quantity lubrication in Ni-based alloy grinding," *International Journal of Machine Tools and Manufacture*, vol. 99, pp. 19–33, 2015.
- [31] M. Yang, C. Li, Y. Zhang et al., "Predictive model for minimum chip thickness and size effect in single diamond grain grinding of zirconia ceramics under different lubricating conditions," *Ceramics International*, vol. 45, no. 12, pp. 14908–14920, 2019.
- [32] B. T. Huang, C. H. Li, Y. B. Zhang et al., "Advances in fabrication of ceramic corundum abrasives based on sol-gel process," *Chinese Journal of Aeronautics*, vol. 34, no. 6, pp. 1–17, 2021.
- [33] M. Yang, C. Li, L. Luo, R. Li, and Y. Long, "Predictive model of convective heat transfer coefficient in bone micro-grinding using nanofluid aerosol cooling," *International Communications in Heat and Mass Transfer*, vol. 125, article 105317, 2021.
- [34] Q. Yin, C. Li, L. Dong et al., "Effects of physicochemical properties of different base oils on friction coefficient and surface roughness in MQL milling AISI 1045," *International Journal of Precision Engineering and Manufacturing-Green Technology*, vol. 8, no. 6, pp. 1629–1647, 2021.
- [35] T. Gao, C. Li, M. Yang et al., "Mechanics analysis and predictive force models for the single-diamond grain grinding of carbon fiber reinforced polymers using CNT nano-lubricant," *Journal of Materials Processing Technology*, vol. 290, article 116976, 2021.
- [36] Z. Duan, C. Li, W. Ding et al., "Milling force model for aviation aluminum alloy: academic insight and perspective analysis," *Chinese Journal of Mechanical Engineering*, vol. 34, no. 1, pp. 1–35, 2021.
- [37] M. Liu, C. Li, C. Cao et al., "Walnut fruit processing equipment: academic insights and perspectives," *Food Engineering Reviews*, vol. 13, no. 4, pp. 822–857, 2021.
- [38] Y. Wang, C. Li, Y. Zhang et al., "Processing characteristics of vegetable oil-based nanofluid MQL for grinding different workpiece materials," *International Journal of Precision Engineering and Manufacturing-Green Technology*, vol. 5, no. 2, pp. 327–339, 2018.
- [39] X. Bai, C. Li, L. Dong, and Q. Yin, "Experimental evaluation of the lubrication performances of different nanofluids for minimum quantity lubrication (MQL) in milling Ti-6Al-4V," *The International Journal of Advanced Manufacturing Technology*, vol. 101, no. 9–12, pp. 2621–2632, 2019.
- [40] C. H. Lee and J. S. Park, "An SDN-based packet scheduling scheme for transmitting emergency data in mobile edge computing environments," *Human-centric Computing and Information Sciences*, vol. 11, no. 28, 2021.
- [41] S. Baek, J. Jeon, B. Jeong, and Y. S. Jeong, "Two-stage hybrid malware detection using deep learning," *Human-centric Computing and Information Sciences*, vol. 11, no. 27, 2021.
- [42] M. Hosseinzadeh Sani, H. Saghaei, M. A. Mehranpour, and A. Asgariyan Tabrizi, "A novel all-optical sensor design based on a tunable resonant nanocavity in photonic crystal microstructure applicable in MEMS accelerometers," *Photonic Sensors*, vol. 11, no. 4, pp. 457–471, 2021.
- [43] M. Hosseinzadeh Sani, A. Ghanbari, and H. Saghaei, "An ultra-narrowband all-optical filter based on the resonant cavities in rod-based photonic crystal microstructure," *Optical and Quantum Electronics*, vol. 52, no. 6, pp. 1–15, 2020.
- [44] H. Dai, J. Li, Y. Kuang, J. Liao, Q. Zhang, and Y. Kang, "Multi-scale fuzzy entropy and PSO-SVM based fault diagnoses for airborne fuel pumps," *Human-centric Computing and Information Sciences*, vol. 11, no. 25, 2021.
- [45] M. Maqsood, I. Mehmood, R. Kharel, K. Muhammad, J. Lee, and W. S. Alnumay, "Exploring the role of deep learning in industrial applications: a case study on coastal crane casting recognition," *Human Centric Computing and Information Sciences*, vol. 11, no. 20, pp. 1–14, 2021.
- [46] M. M. Salim, V. Shanmuganathan, V. Loia, and J. H. Park, "Deep learning enabled secure IoT handover authentication for blockchain networks," *Human-centric Computing and Information Sciences*, vol. 11, no. 21, 2021.
- [47] C. Blundo, C. De Maio, M. Parente, and L. Siniscalchi, "Targeted advertising that protects the privacy of social networks users," *Human-centric Computing and Information Sciences*, vol. 11, no. 18, 2021.
- [48] Y. Zhang, C. Li, D. Jia, D. Zhang, and X. Zhang, "Experimental evaluation of MoS₂ nanoparticles in jet MQL grinding with different types of vegetable oil as base oil," *Journal of Cleaner Production*, vol. 87, pp. 930–940, 2015.
- [49] Y. Wang, C. Li, Y. Zhang et al., "Experimental evaluation of the lubrication properties of the wheel/workpiece interface in

- minimum quantity lubrication (MQL) grinding using different types of vegetable oils,” *Journal of Cleaner Production*, vol. 127, pp. 487–499, 2016.
- [50] L. Xie, Y. Zhu, M. Yin et al., “Self-feature-based point cloud registration method with a novel convolutional Siamese point net for optical measurement of blade profile,” *Mechanical Systems and Signal Processing*, vol. 178, article 109243, 2022.
- [51] M. Yin, Y. Zhu, G. Yin, G. Fu, and L. Xie, “Deep feature interaction network for point cloud registration, with applications to optical measurement of blade profiles,” *IEEE Transactions on Industrial Informatics*, vol. 1, pp. 1–10, 2022.
- [52] Y. Wei, C. Chen, C. Tan et al., “High-performance visible to near-infrared broadband Bi₂O₂Se nanoribbon photodetectors,” *Advanced Optical Materials*, vol. 10, no. 23, article 2201396, 2022.
- [53] P. Gong, D. Wang, C. Zhang et al., “Corrosion behavior of TiZrHfBeCu(Ni) high-entropy bulk metallic glasses in 3.5 wt. % NaCl,” *npj Materials Degradation*, vol. 6, no. 1, p. 77, 2022.
- [54] D. Wang, X. Wang, M. L. Jin, P. He, and S. Zhang, “Molecular level manipulation of charge density for solid-liquid TENG system by proton irradiation,” *Nano Energy*, vol. 103, article 107819, 2022.
- [55] S. A. Esmaili and A. K. Cherri, “Photonic crystal-based all-optical arithmetic circuits without SOA-based switches,” *Optik*, vol. 125, no. 14, pp. 3710–3713, 2014.
- [56] K. Nozaki, E. Kuramochi, A. Shinya, and M. Notomi, “25-channel alloptical gate switches realized by integrating silicon photonic crystal nano-cavities,” *Optics Express*, vol. 22, no. 12, pp. 14263–14274, 2014.
- [57] K. D. Chang and C. Y. Liu, “Electro-optical channel drop switching in a photonic crystal waveguide-cavity side-coupling system,” *Optics Communication*, vol. 316, pp. 10–16, 2014.
- [58] S. Kaur, “All optical data comparator and decoder using SOA-based Mach-Zehnder interferometer,” *Optik - International Journal for Light and Electron Optics*, vol. 124, no. 17, pp. 2650–2653, 2013.
- [59] T. A. Moniem, “All optical active high decoder using integrated 2D square lattice photonic crystals,” *Journal of Modern Optics*, vol. 62, no. 19, pp. 1643–1649, 2015.
- [60] Y. Liu, F. Qin, Z. M. Meng, F. Zhou, Q. H. Mao, and Z. Y. Li, “All-optical logic gates based on two-dimensional low-refractive-index nonlinear photonic crystal slabs,” *Optics Express*, vol. 19, no. 3, pp. 1945–1953, 2011.
- [61] H. Alipour-Banaei, S. Serajmohammadi, and F. Mehdizadeh, “All optical NOR and NAND gate based on nonlinear photonic crystal ring resonators,” *Optik*, vol. 125, no. 19, pp. 5701–5704, 2014.
- [62] Y. Tian, Z. Liu, T. Ying et al., “Experimental demonstration of an optical Feynman gate for reversible logic operation using silicon micro-ring resonators,” *Nano*, vol. 7, no. 1, pp. 333–337, 2018.
- [63] L. Li and G. Q. Liu, “Photonic crystal ring resonator channel drop filter,” *Optik*, vol. 2012, no. 124, pp. 2966–2968, 2019.
- [64] S. Naghizade and S. M. Sattari-Esfahlan, “Excellent quality factor ultra-compact optical communication filter on ringshaped cavity,” *Journal of Optical Communication*, vol. 40, no. 1, pp. 21–25, 2019.
- [65] Z. Zhang, M. Sui, C. Li et al., “Residual stress of grinding cemented carbide using MoS₂ nano-lubricant,” *The International Journal of Advanced Manufacturing Technology*, vol. 119, no. 9-10, pp. 5671–5685, 2022.
- [66] Y. Zhang, H. N. Li, C. Li et al., “Nano-enhanced biolubricant in sustainable manufacturing: from processability to mechanisms,” *Friction*, vol. 10, no. 6, pp. 803–841, 2022.
- [67] X. Cui, C. H. Li, W. F. Ding et al., “Minimum quantity lubrication machining of aeronautical materials using carbon group nanolubricant: from mechanisms to application,” *Chinese Journal of Aeronautics*, vol. 35, no. 11, pp. 85–112, 2022.
- [68] S. Naghizade and S. M. Sattari-Esfahlan, “Loss-less elliptical channel drop filter for WDM applications,” *Journal of Optical Communication*, vol. 40, no. 4, pp. 379–384, 2019.
- [69] H. T. Kim and M. Yu, “High-speed optical sensor interrogator with a silicon-ring-resonator-based thermally tunable filter,” *Optics Letters*, vol. 42, no. 7, pp. 1305–1308, 2017.
- [70] C. Errando-Herranz, F. Niklaus, G. Stemme, and K. B. Gylfason, “Low-power microelectromechanically tunable silicon photonic ring resonator add-drop filter,” *Optics Letters*, vol. 40, no. 15, pp. 3556–3559, 2015.
- [71] R. Talebzadeh and M. Soroosh, “High quality complete coupling 4-channel demultiplexer based on photonic crystal ring resonators,” *Optoelectronics and Advanced Materials, Rapid Communications*, vol. 9, no. 1–2, pp. 5–9, 2015.
- [72] F. Mehdizadeh and M. Soroosh, “A new proposal for eight-channel optical demultiplexer based on photonic crystal resonant cavities,” *Photonic Network Communications*, vol. 31, no. 1, pp. 65–70, 2016.
- [73] M. A. M. Birjandi and M. R. Rakhshani, “A new design of tunable four port wavelength demultiplexer by photonic crystals ring resonators,” *Optik*, vol. 124, pp. 5923–5926, 2014.
- [74] S. Naghizade and S. M. Sattari-Esfahlan, “Tunable high performance 16-channel demultiplexer,” *Journal of Optical Communication*, vol. 41, no. 3, pp. 249–256, 2020.
- [75] B. Youssefi, M. K. Moravvej-Farshi, and N. Granpayeh, “Two bit all-optical analog-to-digital converter based on nonlinear Kerr effect in 2D photonic crystals,” *Optics Communications*, vol. 285, no. 13-14, pp. 3228–3233, 2012.
- [76] A. Tavousi and M. A. Mansouri-Birjandi, “Optical-analog-to-digital conversion based on successive-like approximations in octagonal-shape photonic crystal ring resonators,” *Superlattices and Microstructures*, vol. 114, pp. 23–31, 2018.
- [77] F. Mehdizadeh, M. Soroosh, H. Alipour-Banaei, and E. Farshidi, “Ultra-fast analog-to-digital converter based on a non-linear triplexer and an optical coder with a photonic crystal structure,” *Applied Optics*, vol. 56, no. 7, pp. 1799–1806, 2017.
- [78] F. Mehdizadeh, M. Soroosh, H. Alipour-Banaei, and E. Farshidi, “All optical 2-bit analog to digital converter using photonic crystal-based cavities,” *Optical and Quantum Electronics*, vol. 49, no. 1, pp. 1–1, 2017.
- [79] F. Mehdizadeh, M. Soroosh, H. Alipour-Banaei, and E. Farshidi, “A novel proposal for all optical analog-to-digital converter based on photonic crystal structures,” *IEEE Photonics Journal*, vol. 9, no. 2, pp. 1–11, 2017.
- [80] M. Hosseinzadeh Sani, S. Khosroabadi, and A. Shokouhmand, “A novel design for 2-bit optical analog to digital (A/D) converter based on nonlinear ring resonators in the photonic crystal structure,” *Optics Communications*, vol. 458, article 124760, 2020.
- [81] J. Chen, F. Mehdizadeh, M. Soroosh, and H. Alipour-Banaei, “A proposal for 5-bit all optical analog to digital converter using nonlinear photonic crystal-based ring resonators,” *Optical and Quantum Electronics*, vol. 53, no. 9, pp. 1–9, 2021.

- [82] G. Xin and L. Zhao, "All-optical analog to digital converter based on nonlinear photonic crystal ring resonators," *Photonics and Nanostructures - Fundamentals and Applications*, vol. 41, article 100817, 2020.
- [83] S. Moshfe, M. K. Moravvej-Farshi, and K. Abedi, "Designing an integrated all-optical analog to digital converter," *International Journal of Optics and Photonics*, vol. 14, no. 1, pp. 3–14, 2020.
- [84] A. Shamsi and R. Moradi, "All optical analog to digital converter using nonlinear photonic crystal ring resonators," *Optical and Quantum Electronics*, vol. 52, no. 10, pp. 1–13, 2020.
- [85] M. Mohammadi, F. Habibi, M. Seifouri, and S. Olyaei, "Recent advances on all-optical photonic crystal analog-to-digital converter (ADC)," *Optical and Quantum Electronics*, vol. 54, no. 3, pp. 1–22, 2022.
- [86] S. Rebhi and M. Najjar, "Hourglass nonlinear photonic crystal cavity for ultra-fast all-optical switching," *Optik*, vol. 180, pp. 858–865, 2019.
- [87] W. Zhou, D. Zhao, Y. C. Shuai et al., "Progress in 2D photonic crystal Fano resonance photonics," *Progress in Quantum Electronics*, vol. 38, no. 1, pp. 1–74, 2014.